Title
Seismic response of vertical dry storage casks under three-dimensional earthquake motions

Journal
Nuclear Engineering and Design, 444

ISSN
0029-5493

Authors
Das, Tonmoy
Seylabi, Elnaz
Tabbakhhah, Maryam
et al.

Publication Date
2025-12-01

DOI
10.1016/j.nucengdes.2025.114339

Title: On dynamic response of vertical dry storage casks under three-dimensional earthquake wave fields

Authors: Tonmoy Das[1], Elnaz Seylabi[1], Maryam Tabbakhhah[2], David McCallen[3]

Affiliations: Department of Civil and Environmental Engineering, University of Nevada, Reno, Nevada, United States, 89557 [1], Thornton Tomasetti, San Francisco, California, United States [2], Lawrence Berkeley National Laboratory, Berkeley, California, United States [3]

Corresponding Author: Elnaz Seylabi, elnaze@unr.edu

On dynamic response of vertical dry storage casks under three-dimensional earthquake wave fields

Tonmoy Das[1], Elnaz Seylabi *[1], Maryam Tabbakhhah[2], and David McCallen[3]

[1]Department of Civil and Environmental Engineering, University of Nevada, Reno, Nevada, United States
[2]Thornton Tomasetti, San Francisco, California, United States
[3]Lawrence Berkeley National Laboratory, Berkeley, California, United States

Abstract

Ensuring the seismic safety of dry storage casks (DSCs) has become increasingly critical as these systems evolve into longer-term storage solutions for spent nuclear fuel. This paper presents a high-fidelity modeling framework that leverages the Domain Reduction Method (DRM) and perfectly matched layers (PML) to accurately transfer three-dimensional (3D) simulated earthquake motions from regional-scale fault-rupture models into local-scale finite element analyses of DSCs. Both single-cask (SC) and multi-cask (MC) configurations are evaluated under near-field and far-field scenarios for a generic M_w 7.0 strike-slip event. Emphasis is placed on capturing complex soil-structure interaction (SSI), spatial variability in the ground motion, and nonlinear phenomena such as cask rocking and sliding. Numerical results demonstrate that near-field conditions, where forward directivity and fling-step effects dominate, lead to significantly higher DSC rocking and sliding. Far-field cases, by contrast, generally exhibit modest responses. Incorporating SSI tends to amplify or alter DSC response spectra, underscoring the need for site-specific evaluations and robust modeling approaches to ensure the seismic integrity of DSCs in interim spent fuel storage installations.

*Corresponding author. Email: elnaze@unr.edu

1 Introduction

Spent nuclear fuel generated by nuclear power plants (NPPs) is initially stored in spent fuel pools to manage heat dissipation and prevent cladding damage. After several years, these assemblies are transferred to dry storage casks (DSCs), which are typically housed at Interim Spent Fuel Storage Installations (ISFSIs). Although DSCs are generally licensed for relatively short periods, the suspension of the Yucca Mountain repository licensing and the ease of decommissioning and transportation has effectively transformed them into a longer-term storage solution in the United States.

A DSC is generally a free-standing cylindrical system installed vertically on a reinforced concrete pad. When subjected to strong earthquake ground motions, these characteristics pose stability concerns, including sliding, rocking, tipping potential, and inter-cask collisions [1, 2, 3]. Consequently, numerous studies have investigated the seismic response of DSCs through a combination of numerical simulation and shake-table experimentation. Broadly, these works have focused on (i) the effect of friction at the cask-pad interface on sliding and rocking [3, 4], (ii) the role of vertical accelerations in promoting partial uplift [5, 6], (iii) the influence of soil properties on cask displacements and tipping risk [7], and (iv) the complex behavior of free-standing casks under multi-directional ground motions [8, 9]. Parallel researches on fragility analysis has also concluded that while tipping and canister failure probabilities can be extremely low, certain sites and seismic scenarios pose a heightened risk of exceeding allowable rocking angles [10, 11].

Because DSCs rest directly on a concrete pad above a soil foundation and are low-rise and stiff, soil-structure interaction (SSI) has emerged as a key factor in their seismic performance. Several early studies demonstrated that the flexibility of the pad can significantly affect cask responses, often leading to amplified accelerations and displacements if the pad is relatively thin [7, 12]. Subsequent numerical analyses refined these findings by examining multi-cask layouts, variable soil profiles, and frictional contact at the pad-cask interface [8, 13, 14], but generally relied on one-dimensional (1D) deconvolution methods or simplified boundary conditions to approximate vertically propagating shear waves. These simplifications are computationally attractive yet neglect the complexities of truly three-dimensional (3D) wave propagation—particularly relevant for near-fault excitations and multi-component ground motions.

The present study aims to address these limitations by developing a higher-fidelity modeling framework that captures 3D seismic wave fields, including inclined body and surface waves, and advanced SSI effects. Specifically, it employs perfectly matched layer (PML) elements and the Domain Reduction Method (DRM) to transfer simulated regional-scale earthquake motions into local-scale finite element models of the soil-cask system. Unlike conventional large-domain or soil-spring approaches, this DRM-based technique accommodates spatially varying ground motion components in three dimensions while mitigating artificial wave reflections at model boundaries. Additionally, the DSC is explicitly modeled with sufficient detail to resolve global structural behavior, including center-of-gravity (CG) accelerations and any potential rocking-sliding interaction. By examining both near-field and far-field earthquake scenarios, as well as fault-parallel versus fault-normal motion components, this research offers a more comprehensive characterization of DSC seismic performance.

The paper is organized as follows: Section 2.1 provides details on generating 3D earthquake wavefields using the EQSIM framework [15]. Then, Sections 2.3 and 2.4 discusses the steps adopted to perform the finite element modeling the response of single and multi-casks under 3D earthquake wavefields using the DRM. Finally, Section 3 presents the results with the concluding remarks provided in Section 4.

2 Modeling approach

This section summarizes our two-scale coupling approach to model the response of DSCs under 3D seismic wavefields. Section 2.1 outlines the details of the EQSIM framework for generating the 3D earthquake wavefields and Section 2.2 presents our assumptions to develop the localized soil island in LS-DYNA, taking advantage of the DRM and PML. Lastly, Sections 2.3 and 2.4 describes the finite element models for single and multi-cask settings.

2.1 Modeling synthetic 3D earthquake wavefields

To generate the 3D earthquake wavefields, a generic M_w7.0 central hypocenter seismic event with a strike-slip fault was considered in the EQSIM framework. The EQSIM (EarthQuake SIMulation) is a multidisciplinary platform that leverages the power of high-performance computing to facilitate regional-scale 3D fault-to-structure simulation, enabling risk-informed decision-making for critical infrastructure. The core engine of EQSIM is SW4 (Seismic Waves, 4th order), a summation-by-parts finite difference code for solving the viscoelastic wave equation, optimized to work with massive parallel computing architecture [16, 17].

SW4 achieves fourth-order accuracy in space and time, ensuring highly accurate representations of complex earthquake wavefields. It is extensively verified and offers advanced capabilities, including topography-following curvilinear grids, efficient deep-region Cartesian grids, far-field absorbing boundaries, anelastic attenuation for realistic energy dissipation, and 3D heterogeneous material models. These features allow the simulation of fully deterministic, broadband synthetic motions comparable to real earthquake records [18]. For a more detailed overview of the framework, readers are referred to [15].

Figure 1a shows the idealized 100km×40km×30km computational domain with a free flat 600m deep canonical shallow basin model. The basin's shear wave velocity (V_s) increases incrementally from 353m/s at the free surface to 800m/s at the base. The variation of the material properties for the simulation is modeled using the equations provided herein:

$$
\begin{aligned}
V_p(z) &= 1000 + 1.2z \text{ (m/s)} \\
V_s(z) &= 320 + 19\sqrt{z} \text{ (m/s)} \\
\rho(z) &= 2140 + 0.125z \text{ (kg/m}^3\text{)} \\
q_p(z) &= 80 \\
q_s(z) &= 40
\end{aligned} \tag{1}
$$

where z is depth, V_p and V_s are the longitudinal (P-wave) and shear wave (S-wave) velocities, respectively, ρ is density, and q_s and q_p represent the quality factors, indicating attenuation of shear and longitudinal waves passing through the basin. Additional modeling assumptions, including the details of the surrounding rock, are explained in [19].

The fault, extending 62.5km in length and 16km in width, with its hypocenter at 9km depth, ruptures to 200m below the surface and is located next to the rock-basin interface. The rupture scenario is modeled using the Graves-Pitarka kinematic rupture technique [20] with spatial slip rate enhancement [21]. Consistent with observations from mature crustal faults, the rupture velocity was set to 80% of the local shear wave velocity alongside an average rake angle of 0° with allowance of random spatial perturbations.

As shown in Figure 1a, the study considers five different sites positioned in the XY plane to assess DSC behavior under both near- and far-field earthquake scenarios. Site A (50, 15) and B (50, 20), situated respectively 5km and 10km from the fault, represents near-field conditions, while Site C (50, 35), D (25, 35), and E (75, 35) reflects far-field cases. The latter three sites, each situated at a primary distance of 25km from the fault, maintain an additional inter-site spacing of 25km. All locations identified here are measured in km from the origin of the XYZ coordinate system shown in Figure 1a.

The ground motion simulations were configured to resolve frequencies up to 5Hz while

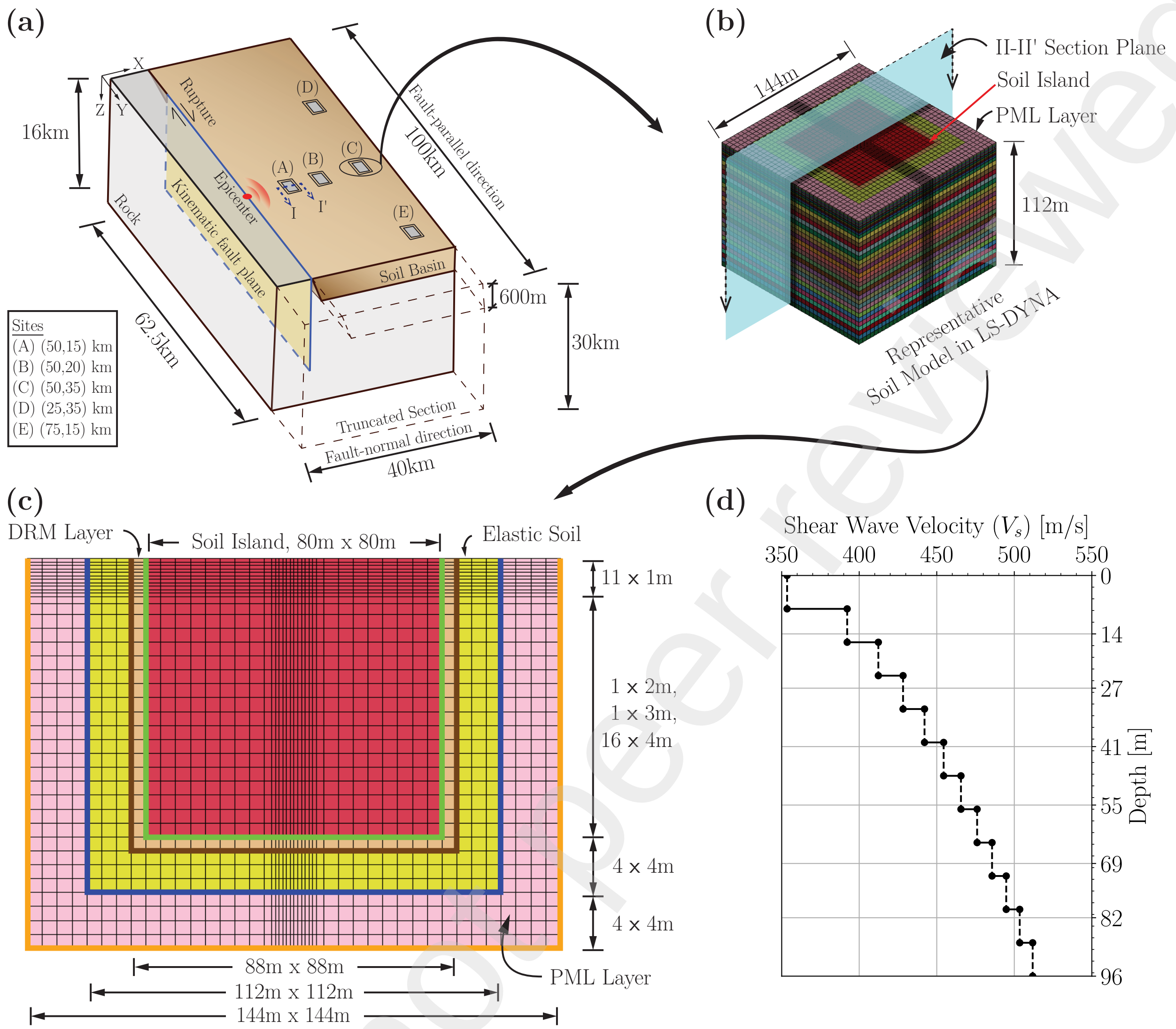

Figure 1: The (a) 100km×40km×30km idealized computational domain showing site locations with a (b) snippet of the whole soil domain (c) cross-section of the soil model at II-II', and (d) shear wave velocity (V_s) of the soil island, DRM and elastic soil layers.

maintaining a minimum of eight grid points per shortest wavelength. This reflects the computational constraints of 3D wave propagation modeling, where doubling the maximum frequency resolution requires a sixteen-fold increase in computational resources.

2.2 Modeling the soil island

The soil domain was modeled using a direct approach with a soil island of dimensions 80m × 80m × 80m in LS-DYNA (Figure 1b and c), implementing linear elastic solid elements.

As material nonlinearity was beyond the scope of this study, the initial aspect ratio remained constant, eliminating potential problems regarding shear locking [22]. Hence, full integration techniques were employed for the 8-node hexahedral elements. The discretizations of the layered soil was carried out incrementally, with the central domain comprising elements of 1m dimension and the outer domain utilizing 4m elements. Figure 1c presents the 17 distinct layers within the DRM model with their corresponding dimensions. The shear wave velocity (V_s) obtained in the elastic soil domain region (up to 96m from the surface) is illustrated in Figure 1d.

The DRM layer, positioned immediately outside the soil island, was generated with a 4m grid spacing. Material properties, namely the elastic modulus, Poisson's ratio, and density, assigned to the DRM model were identical to those implemented in the SW4 code. SSI interface keywords were defined at inner and outer DRM layer boundaries to specify ground motion application locations. The soil island and DRM layer were encapsulated by four bands of PML elements, where the PML utilized material properties from its adjacent bounded layer. PML serves as an advanced non-reflecting boundary for linear wave equations, providing near-perfect absorption of outgoing waves across nontangential incidence angles and non-zero frequencies [23]. Its mathematical formulation incorporates complex coordinate stretching within the elastic wave equation, enabling complete absorption of waves at all frequencies and incident angles without reflection at the interface. This local formulation distinguishes PML from traditional absorbing boundaries, offering superior performance through wave attenuation within the layer. As a result, these elements can effectively simulate unbounded domain behavior with minimal wave reflection [24].

The *DAMPING_FREQUENCY_RANGE_DEFORM keyword with a coefficient of 0.0078125 was also implemented using Equation (2) across the $1 - 10$ Hz frequency range to model the small strain damping, with the q_s being consistent with Equation (1).

$$\xi = \frac{1}{2q_s} \tag{2}$$

As it will be discussed later, this modeling approach offers twofold advantages: it enables the direct generation of free-field ground motions for uncoupled fixed-base models, identified as the No-SSI case, while also enabling a straightforward SSI incorporation by placing the DSCs on the surface of the soil island.

2.3 Modeling the single cask system

The considered DSC has four main components: inner and outer steel shells, concrete shielding between the shells, the spent fuel canister assembly, and a base plate. However, a simplified model was implemented for all analyses, omitting the internal components to assess global SSI behavior while reducing computational demands. To ensure the dynamic characteristics of the simplified model reflect the considered DSC, a group of modal analyses were carried out to achieve the equivalent mass, center of gravity (CG), and stiffness. The final system consisted of two components - the bottom part with a height of 0.56m and a top part with a height of 5.15m consisting of a total mass of $147,117$kg and a radius of 1.73m.

The contact surface between the DSC and the foundation pad underneath was modeled using an automatic surface-to-surface contact algorithm considering the static (μ_s) and dynamic (μ_k) frictional coefficients of 0.74 and 0.6, respectively. This penalty-based contact definition introduces stiff springs between the two interacting surfaces (i.e., SURFA and SURFB) to prevent penetration. For a concrete pad with light to medium sandblast finish, μ_s was found to be 0.74 ± 0.035 and μ_k as 0.60 ± 0.046, according to the 48 pull-off tests conducted in [25].

Several options are available to model small-strain material damping beyond frictional energy dissipation to suppress numerical noise at higher frequencies. For this study, a composite damping model was adopted, combining mass proportional Rayleigh Damping with a damping constant of 0.25 and frequency-independent damping with a coefficient of 0.005 by inserting the *DAMPING_PART_MASS and *DAMPING_FREQUENCY_RANGE_DEFORM cards respectively in the input deck. This configuration targets 0.5Hz to 50Hz frequency range, achieving approximately 1% constant damping at the element level, while preserving rigid body motions by activating the DEFORM option.

The elements of the foundation pad with a dimension of 5m×6m×0.15m and the DSC were generated with the linear elastic material model *MAT_ELASTIC considering fully-integrated 8-node hexahedral solid elements. The material properties, namely the elastic modulus (E), density (ρ) and Poisson's ratio (ν), can be found in Table 1.

Table 1: Material properties used to generate the DSC model

Part Name	ρ (kg/m^3)	E (GPa)	ν
Foundation Pad	2400	2.43	0.2
Cask Top Part	2830.5	32.88	0.2
Cask Bottom Part	2400	32.88	0.2

For SSI analyses, the cask and the foundation pad are attached to the top center of the soil surface using a constraint-based surface-to-surface tied contact scheme. This contact algorithm was selected based on [8], who demonstrated that bonded interfaces between concrete pad and soil tend to amplify the responses of DSCs, rendering the most adverse condition. The DRM motions, extracted from the EQSIM computational domain presented in Section 2.1, were specified at the outer interface of the soil island as acceleration time histories using *INTERFACE_SSI keyword card. The generated finite element model is presented in Figure 2.

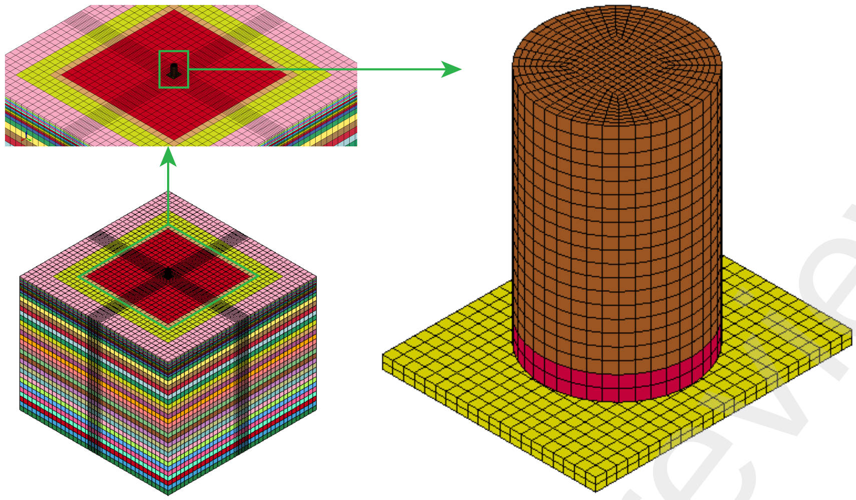

Figure 2: Developed single cask model on the surface of the soil island.

2.4 Modeling the multi-cask system

A separate foundation pad with a dimension of 61.5m×9.5m×0.91m was constructed for the models with multiple DSCs (MC) to reflect more realistic ISFSI conditions. An array of 2×13 single DSC (SC) was arranged in a grid pattern with a CG to CG distance being 4.72m×4.72m with 0.67m edge distance. Each SC of the array retained the same dimensional and material properties outlined in Table 2. The *CONTACT_AUTOMATIC_SURFACE_TO_SURFACE definition was updated to handle interactions between each DSC and the surface of the concrete pad modeled underneath, ensuring accurate force transfer and accounting for potential overlaps. For the MC SSI model, the implemented tied contact algorithm for the SC was expanded to account for the larger pad interface and attachment to the soil domain. This approach allowed for a direct comparison under the same loading conditions, facilitating an analysis of how introducing MC impacts deformation patterns, load distribution, and responses of a typical ISFSI system.

The original MC model was transformed so that the long direction of the foundation pad was oriented in parallel to the X-axis of the global coordinate shown in Figure 1a, forming the MC model oriented in the fault-normal (FN) direction, or the MC FN No-SSI case. Conversely, the foundation pad was reoriented to position its long direction parallel to the global Y-axis, establishing the fault-parallel configuration, or the MC FP No-SSI model. Both configurations were placed on the soil island, as shown in Figure 3, creating the coupled MC FN and MC FP SSI models. With a similar procedure described in Section 2.1, DRM motions were applied at the soil interface to perform the SSI analyses.

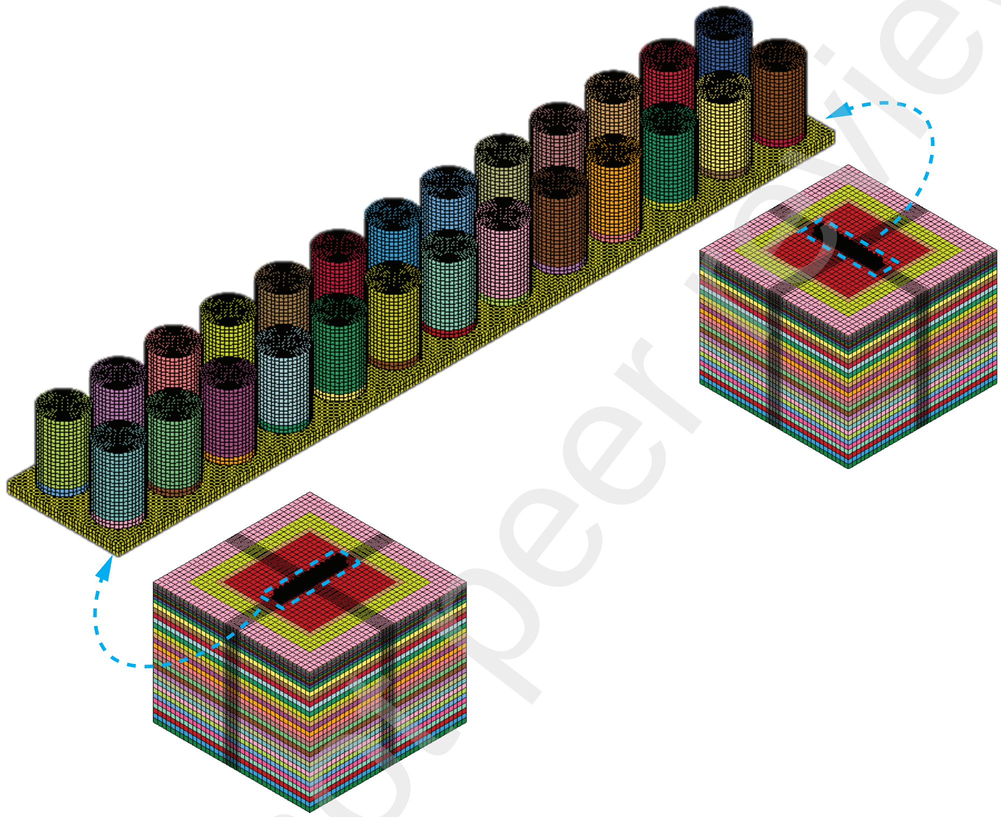

Figure 3: Developed MC models for FN SSI (bottom left), FP SSI (bottom right), and DSCs configuration (top) to use in all three cases.

The response analysis of DSCs exhibits significant nonlinearity, primarily due to rocking, impacts at contact surfaces, and sliding behaviors. Hence, explicit time integration scheme was adopted for both fixed- and flexible-base DSC analyses. Furthermore, LS-DYNA's efficient parallelization capabilities through the Message Passing Interface, robust material models, and seamless integration with the EQSIM, using DRM and PML, made it an attractive candidate for this application. All computations were carried out on a server using 32 cores of AMD EPYC 7763 with 1TiB memory and the consistency flag turned on.

3 Results and discussion

3.1 Free field motion characteristics

To verify the developed workflow of coupling the 3D earthquake wavefields generated using SW4 with the LS-DYNA model using the DRM, we used the developed soil island to generate the free-field motion and compare it against the SW4 results. Due to the absence of localized features within the soil island, the developed model in LS-DYNA under DRM motions should generate the same ground motions as the one simulated using the SW4. Figure 4 compares the generated free-field motions at the center point on the surface of the soil island for Site (A) from Figure 1a. The excellent agreement in all three directions confirms the accuracy of the developed model and the correct implementation of the DRM motions from the local-scale finite element model. It is worth noting that the results at other sites have achieved similar accuracy and are excluded for brevity.

As shown in Figure 4, near-field strike-slip seismic events (i.e., Sites (A) and (B)), exhibit characteristic displacement signatures. These include permanent ground deformation ("fling step") in the fault-parallel direction and long-period, high-amplitude pulses ("forward directivity effect") in the fault-normal direction during arrival of the motions, aligning with the observations of [26].

Table 2: Hazard Overview of All Five Rupture Distances

Considered Sites	PGA (g)			PGV (m/s)			PGD (m)			Real World Counterpart [27]
	X	Y	Z	X	Y	Z	X	Y	Z	
A	0.43	0.56	0.18	0.71	0.62	0.21	0.57	0.75	0.17	Hanford NPP
B	0.21	0.66	0.15	0.32	0.70	0.21	0.37	0.55	0.09	Palo Verde NPP
C	0.07	0.18	0.06	0.15	0.28	0.07	0.12	0.16	0.04	–
D	0.10	0.24	0.06	0.15	0.32	0.06	0.16	0.15	0.03	–
E	0.08	0.28	0.07	0.09	0.35	0.08	0.08	0.30	0.03	–

Table 2 presents an overview of the hazard levels at all five sites. Among them, we can observe that the free-field motion at Site (A) is more dominant with the peak ground acceleration (PGA) of 0.43g in the X-direction. On the contrary, the Y-direction PGA and

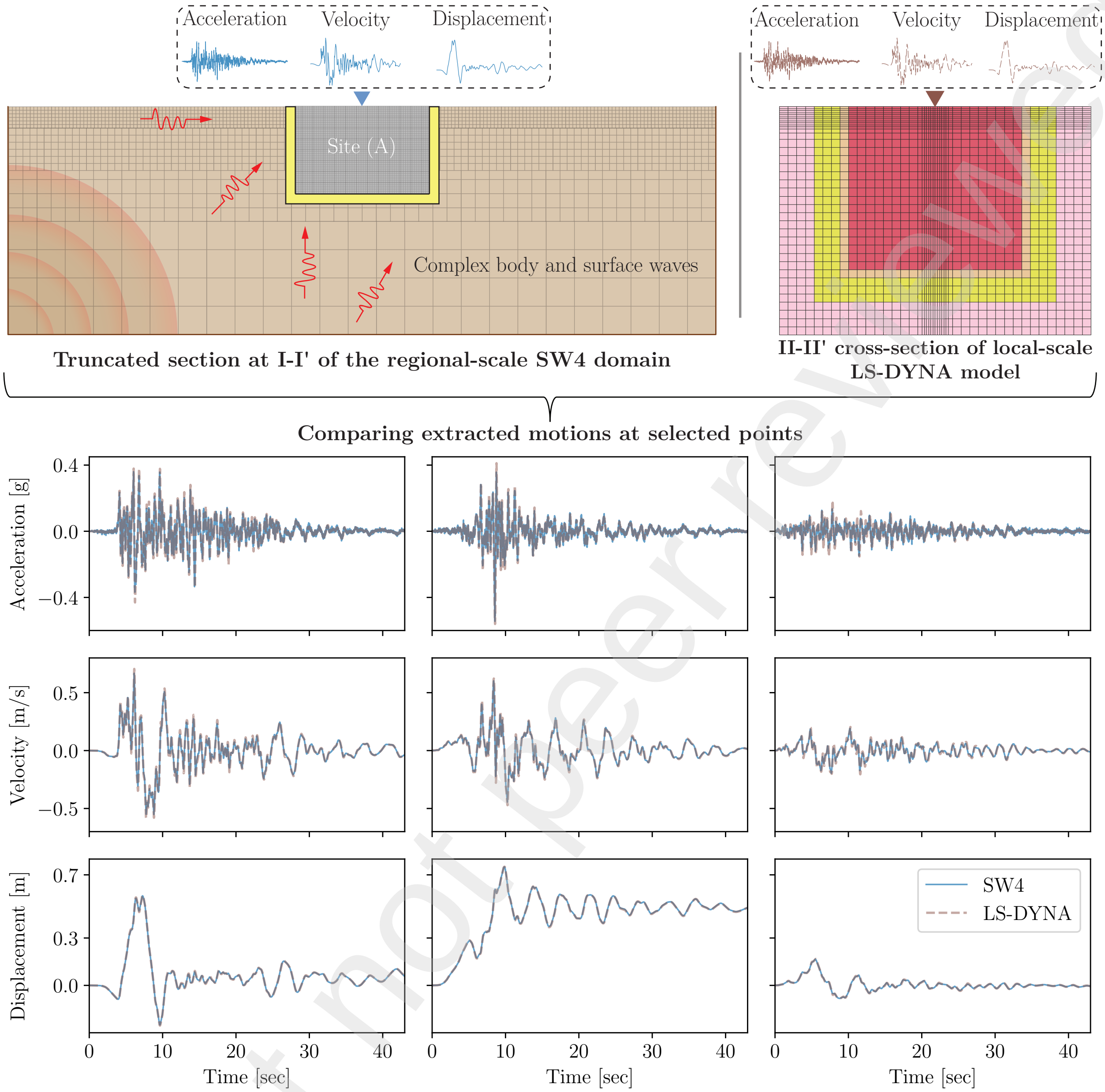

Figure 4: Comparison of free-field responses between regional-scale SW4 (top left) and local-scale LS-DYNA (top right) models at Site (A) across (bottom) X/FN (column 1), Y/FP (column 2), and Z/V (column 3) directions.

peak ground velocity (PGV) are higher for the free-field motion at Site (B), but the peak ground displacement (PGD) is lower than in Site (A). The PGAs and PGVs of the far-field sites (C-E) are significantly lower in all three directions. In contrast, their Y-directional motions are comparable with the X-directional free-field responses at site (B).

Figure 5 portrays the ratio of pseudo spectral acceleration (PSA) to PGA of free-field motions at the considered sites, compared with three different design PSA/PGA prescribed by the US Nuclear Regulatory Commission (NRC) regulatory guidelines [28, 29, 30]. We can observe that the PSA/PGA ratios of the considered sites exceed the NUREG CR6728 design spectra across a broad frequency range but in better agreement with the NUREG 1.60 and CR0098 design spectra. Disagreements are particularly noticeable in the 2-4 Hz range, where the considered free-field responses reach values 1.5-3 times higher than the design spectra.

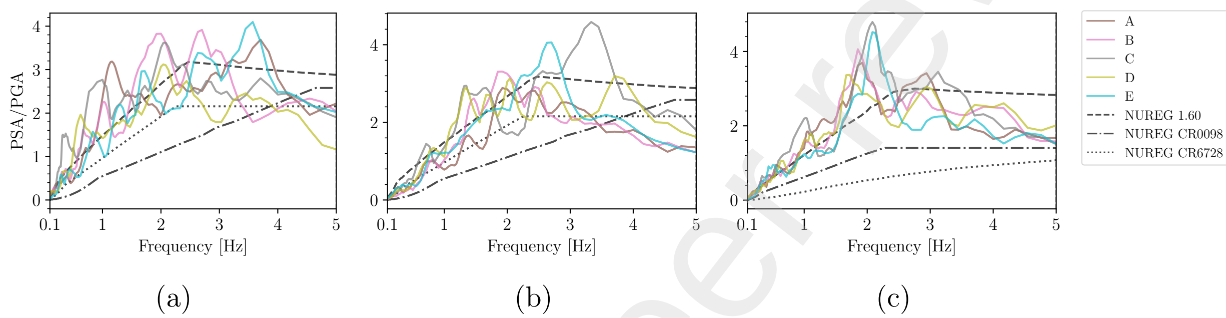

Figure 5: PSA/PGA of the obtained free-field ground motions in (a) X, (b) Y and (c) Z directions against NUREG–1.60 [28], NUREG–CR0098 [29] and NUREG–CR6728 [30].

3.2 Single cask response characteristics

This section discusses the response characteristics of a single cask in terms of CG-level response spectra, sliding, and rocking. Due to the rigidity of the structure, the cask is expected to follow the foundation pad motions before sliding or rocking.

3.2.1 CG-level response spectra

Figure 6 shows the acceleration response spectra for the input free field motions and CG-level accelerations for the single cask No-SSI and SSI cases, compared in each direction. The dashed vertical lines at 0.3, 0.8, 1.3, 1.8, 2.3, 2.8, 3.3, 3.8, 4.3, and 4.8 Hz represent the natural frequencies of a 1D slice of the basin structure considered in this study. Since the generated earthquake wave fields are resolved up to 5Hz, the following discussions will be limited to the response characteristics observed from 0.1 to 5Hz. As evident, the spectral accelerations amplifications in free-field cases show correlations with the computed natural frequencies of the basin.

Generally speaking, the far-field cases follow the free-field spectra closely due to a lower level of ground motion intensity, while the near-field cases exhibit significant amplifications. These response characteristics agree with the sliding and rocking trends discussed in the next section.

The SSI analysis for far-field sites, (C)-(E), shows a more pronounced response amplification at the predominant 2–4Hz input frequency than the fixed-base analysis, especially for the two horizontal components. In the near-field sites, for the intermediate distance (B), the difference between the SSI and No-SSI cases is more noticeable than in site (A), suggesting the complex dynamic behavior induced by taking SSI into account.

3.2.2 Rocking and sliding

The rocking angle is measured as the angle between the axis of the cylindrical DSC and the normal established at the center of the cask base in its initial position. The relative sliding response of the casks can be described as the horizontal displacements of the center of the base surface of the modeled DSC relative to the center of the top surface of the storage pad. It is important to note that this interpretation ignores the pad's elastic deformation. However, analysis suggests that the contribution of elastic pad deformations to the relative horizontal displacement between a cask and any selected point on the pad surface is insignificant compared to the relative sliding displacement. The rocking and sliding for far-field cases, sites (C)-(E), were negligible and are not presented here.

As shown in Figure 7, for Site (A), 5km from the fault, the rocking reaches approximately 3.95° for the SSI configuration, indicating a 25% increase than the No-SSI case. Site (B), situated 10km from the fault rupture, demonstrates a similar trend; however, the rocking angle for the SSI case does not exceed 3° this time, marking 15% higher rocking than the

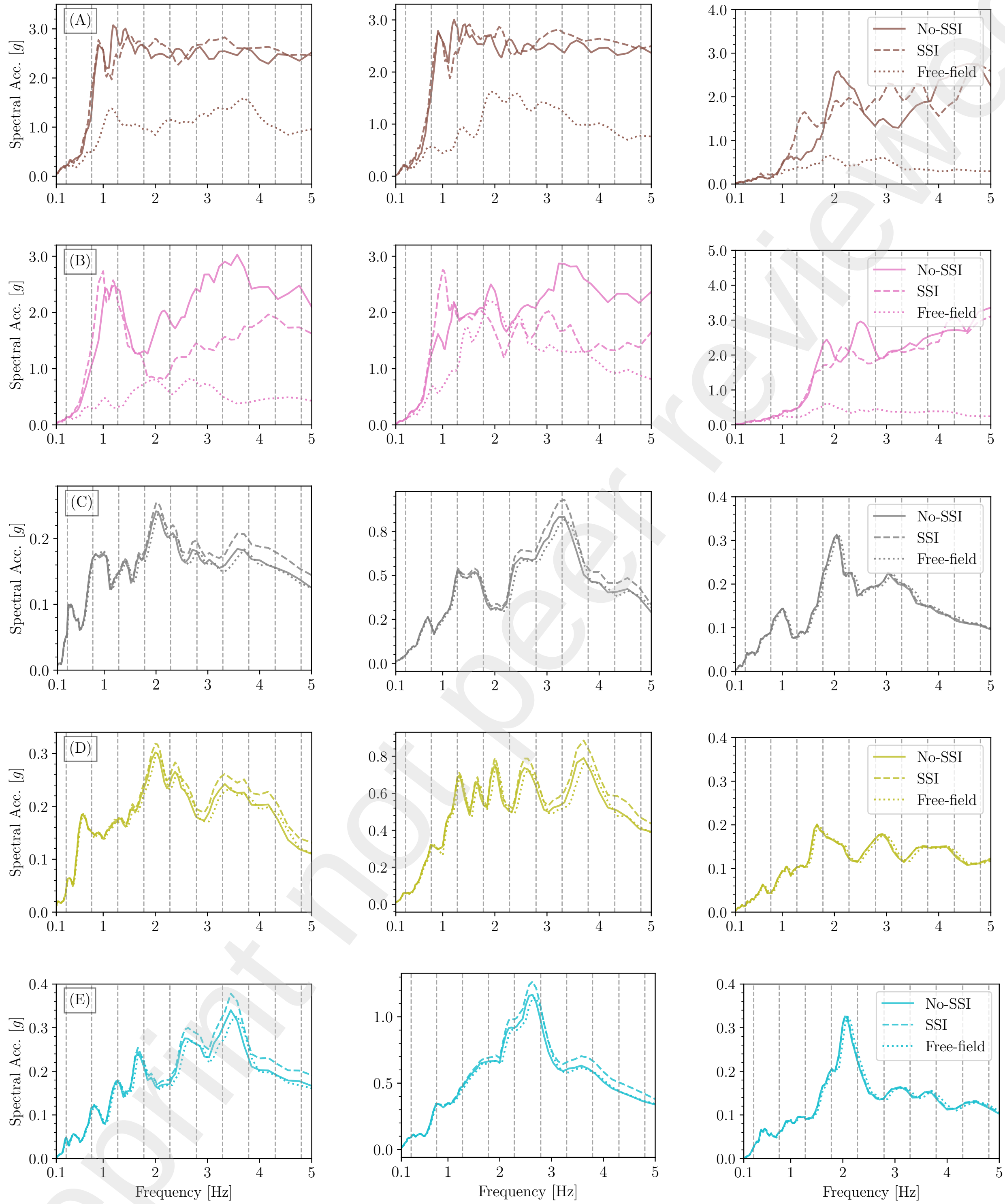

(a) X (b) Y (c) Z

Figure 6: Comparison of acceleration response spectra for SC No-SSI and SC SSI at the CG level against the free-field in (a) X, (b) Y and (c) Z directions (dashed vertical lines indicate the natural frequencies of the sedimentary basin).

No-SSI DSC.

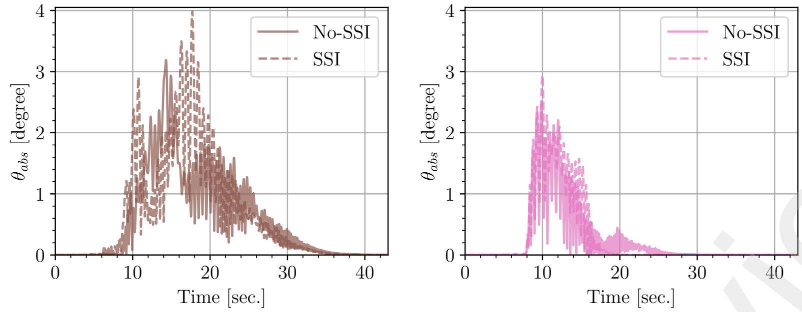

(a) Site (A) (b) Site (B)

Figure 7: Rocking responses comparison for the SC No-SSI and SC SSI for sites (A) and (B) in terms of absolute value (abs) of rocking angle (θ).

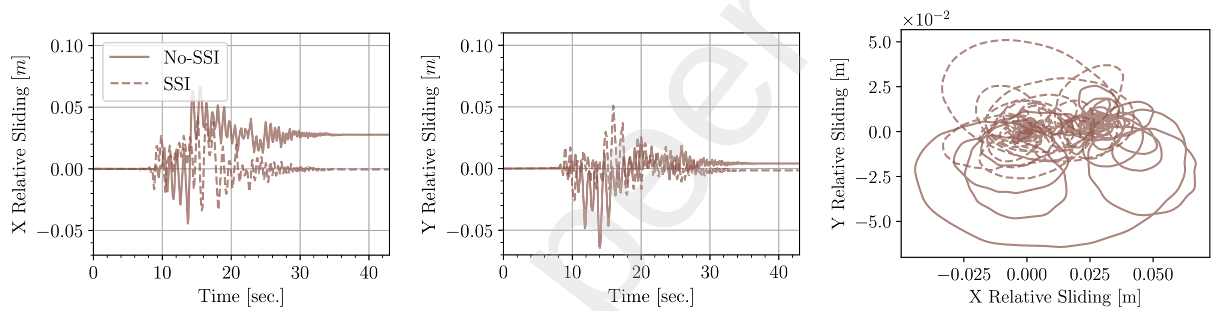

(a) Site (A)

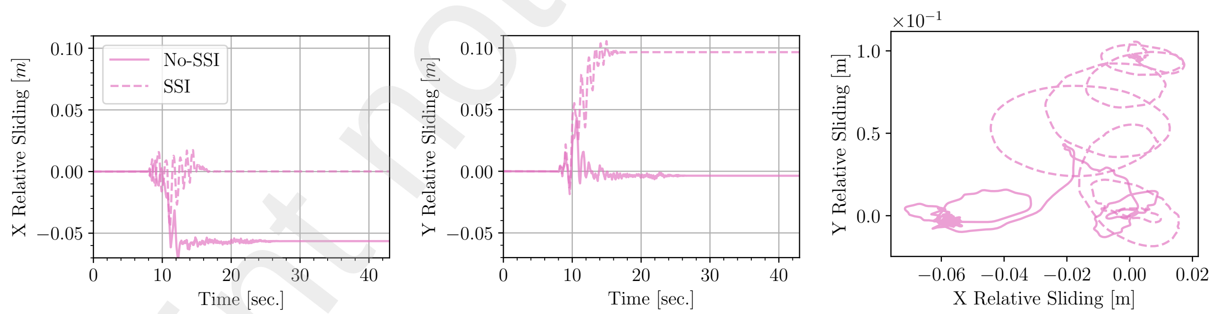

(b) Site (B)

Figure 8: Sliding responses in the horizontal directions for the SC model and their traces without and with SSI effects for Sites (A) and (B).

As illustrated in Figure 8, the sliding starts at a timestamp close to rocking initiation. Although the rocking patterns of the SSI and No-SSI cases are pretty similar, especially for Site (B), their sliding patterns deviate significantly from each other. This underscores the highly nonlinear behavior of the free-standing vertical casks where changes in the input motion due to SSI can significantly affect rigid body responses. Nevertheless, the maximum relative sliding for SC DSCs did not exceed 11cm for the cases considered.

3.3 Multi cask response characteristics

This section discusses casks' response characteristics in MC settings to determine how SSI may affect their dynamic behavior in terms of foundation pad and CG-level response spectra, sliding, and rocking.

3.3.1 Pad-level response spectra

The multi-cask setting comprises 26 casks; therefore, 26 pad-level acceleration responses are measured under each configuration. To better demonstrate the scatter of the pad-level acceleration response spectra compared to the free-field motions discussed in Section 3.1, we compute the mean and the standard deviation of the 26 pad-level spectral accelerations at each frequency.

Figure 9 compares the results of FN and FP configurations for No-SSI and SSI cases. As expected, in both near and far-field cases, the pad-level response spectra are comparable to the free-field response spectra in both horizontal directions. The No-SSI cases' results again agree with the free-field case for the vertical direction. This is because the foundation pad is relatively rigid, and all nodes at the base move together following the free-field motion. For SSI cases, on the other hand, the FP case, followed by the FN case, shows variations in the vertical direction, demonstrating the pad rocking due to spatial variability of the 3D earthquake wave field at the footprint of the foundation pad.

3.3.2 CG-level response spectra

Figure 10 presents the CG-level acceleration spectra for all the FN and FP MC configurations compared to SC No-SSI and SSI cases. As shown, the near- and far-field cases show different

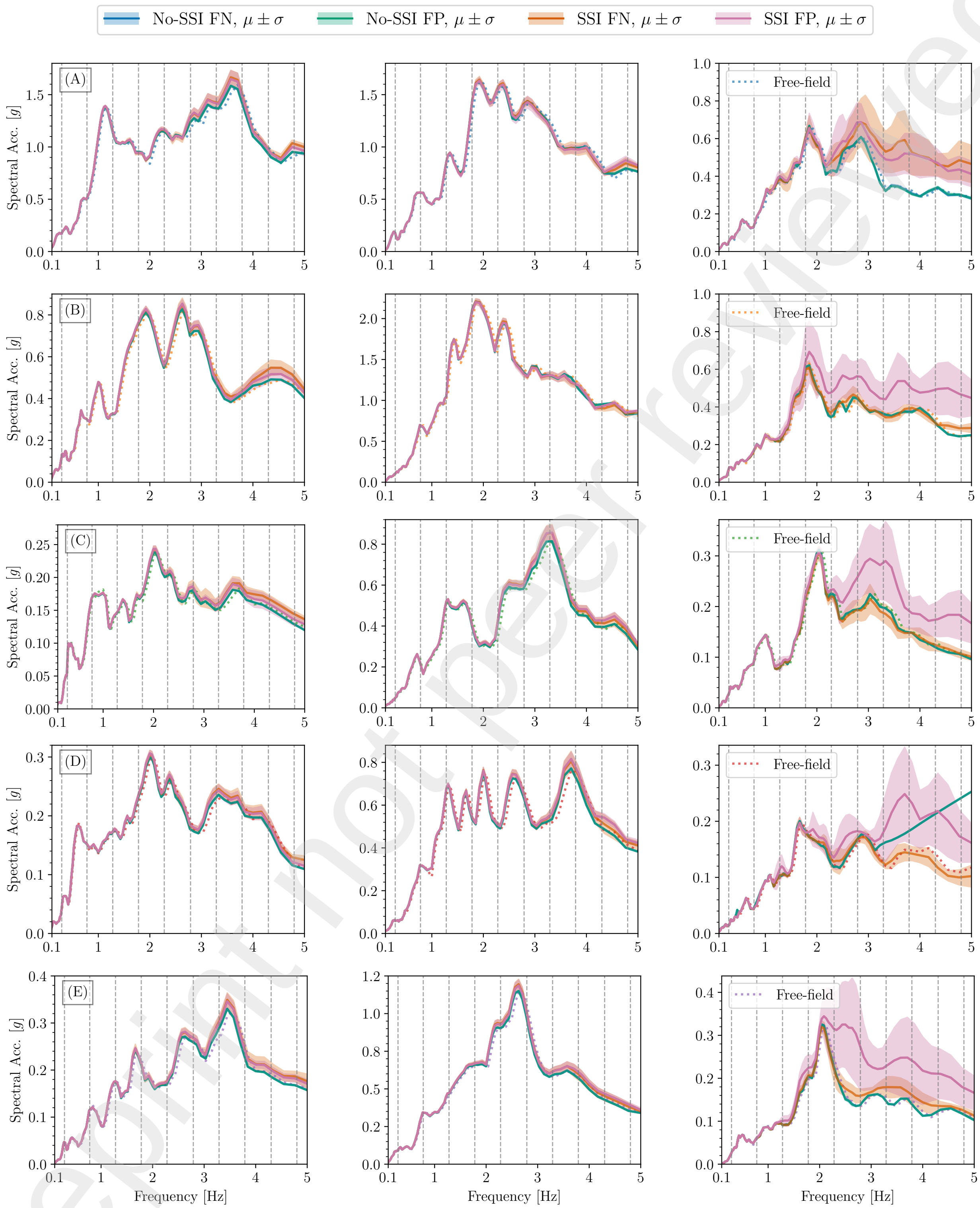

(a) X (b) Y (c) Z

Figure 9: Comparison of spectral acceleration of the free-field with the mean (μ) and standard deviation (σ) of responses obtained from the MC models' concrete pad for sites (A)-(E) (dashed lines indicate basin natural frequencies).

response characteristics.

At far-field sites, the CG-level response spectra closely match the pad-level responses presented in Figure 9. This similarity arises primarily because the seismic intensities were insufficient to initiate sliding or rocking in the far-field cases considered in this study. Conversely, CG-level responses exhibit noticeable variations and amplifications at near-field sites in all three directions compared to the pad-level responses. These discrepancies result mainly from induced rocking and sliding behaviors, which are discussed in detail in the subsequent section.

Additionally, the observed reduction in cask CG-level response, relative to the MC No-SSI case for both FN and FP scenarios, can be attributed to energy dissipation associated with SSI. Moreover, comparing MC SSI models against the No-SSI cases, the latter shows less scatter in CG-level response spectra. This variance suggests that sliding and rocking motions demonstrate more significant variability in the SSI cases compared to the No-SSI configurations. These differences in response characteristics can be attributed to the kinematic, and subsequent inertial, interaction in the SSI analysis.

3.3.3 Maximum sliding and rocking patterns

The maximum resultant relative sliding responses and maximum absolute rocking angles for each DSC were plotted simultaneously to facilitate a clear interpretation of their responses. This comprehensive visualization enables a better understanding of energy dissipation mechanisms and potential correlations between maximum sliding and rocking responses for specific scenario.

In Figures 11 to 14, the initial cask positions are denoted by gray dashed circles, while arrows indicate cask displacement from the original to the final center positions. To enhance the visibility of the relatively small sliding displacements compared to overall system dimensions, a displacement scale factor (DSF) of 8 is applied to generate the illustrations. Each cask is color-coded according to its maximum experienced rocking angle, with an accompanying color

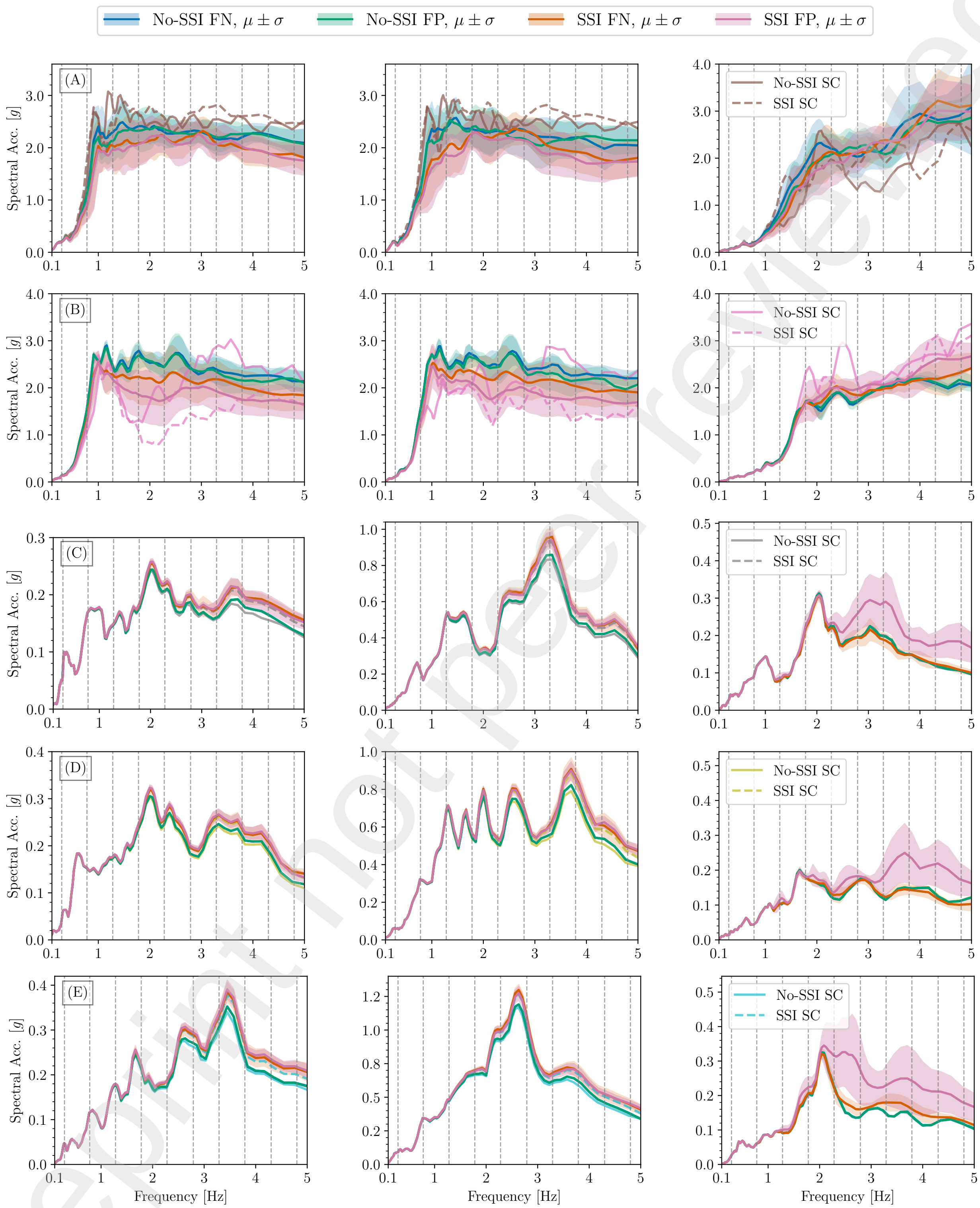

(a) X (b) Y (c) Z

Figure 10: Response Spectra comparison of CG level acceleration responses for the MC mean (μ), and standard deviation (σ) with the SC models for sites (A)-(E) (vertical dashes indicate basin natural frequencies).

bar indicating the range. We note that the resultant relative displacement and maximum rocking may occur at different time instances during the simulation.

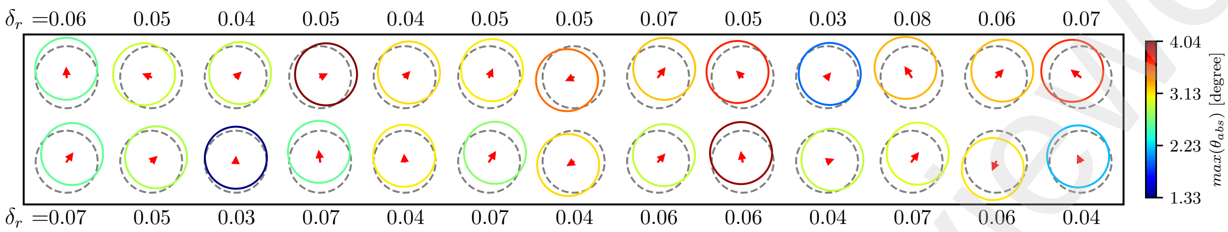

(a) Site (A)

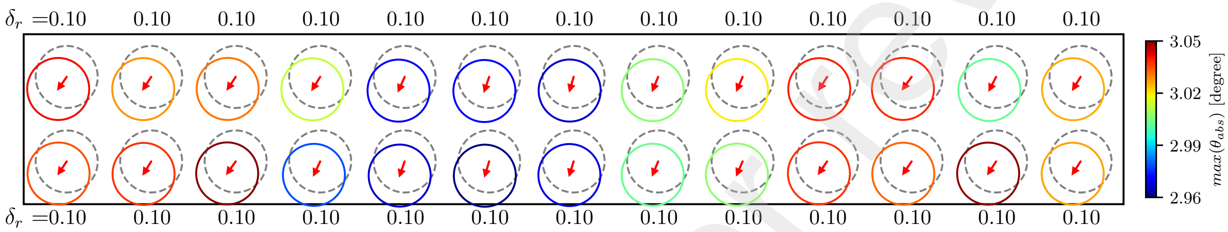

(b) Site (B)

Figure 11: Plan view: maximum resultant sliding vectors (δ_r, visualized with DSF 8) and maximum absolute rocking ($max(\theta_{abs})$) responses of DSCs for FN No-SSI case.

Figure 11a provides an overview of the resultant sliding and maximum rocking observed for each DSC at Site (A) for the No-SSI FN case. The response patterns demonstrate notable variability, with some casks exhibiting high sliding and rocking at the same instance, while others show opposite relationships between these parameters. The two casks at the center of the concrete pad demonstrate moderate sliding and rocking, whereas three of the four DSCs positioned at the two opposite edges of the pad experience maximum sliding and/or rocking amplitudes. For Site (B), presented in Figure 11b, the DSCs exhibited uniform rocking and sliding responses with consistent directional patterns. This behavior aligns with theoretical expectations for fixed base No-SSI conditions, where fixed-base analysis combines identical natural frequencies across all DSCs and uniform ground motion input.

A similar observation can be made for the FP No-SSI configurations, illustrated in Figure 12, with variance in the rocking and sliding for Site (A) and uniformity of responses for Site (B). For Site (A), compared to the fixed based FN No-SSI analysis, the FP orientation exhibits

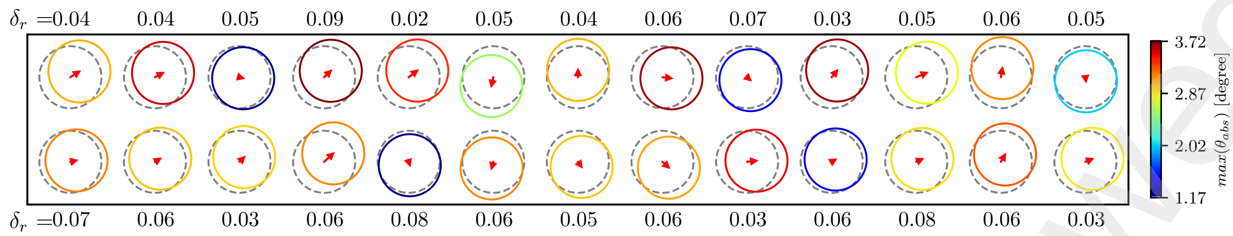

(a) Site (A)

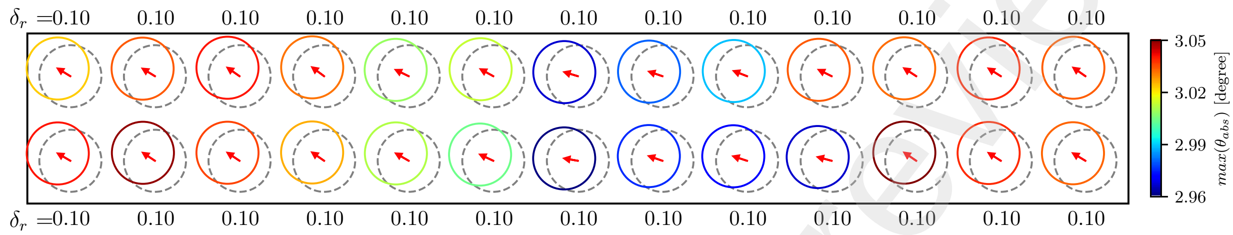

(b) Site (B)

Figure 12: Plan view: maximum resultant sliding vectors (δ_r, visualized with DSF 8) and maximum rocking responses ($max(\theta_{abs})$) of DSCs for FP No-SSI case (transformed counter-clockwise).

higher response variability, with coefficients of variation (CV) of 0.262 for rocking and 0.307 for sliding, compared to 0.193 and 0.250 respectively for the FN case. This translates to percent differences between maximum and minimum values of 219% for rocking and 247% for sliding in the FP orientation, versus 204% and 176% in the FN orientation. As discussed, Site (B) displays comparatively uniform responses in No-SSI configurations, with CVs below 0.015 for both rocking and sliding. The percent differences between maximum and minimum values at Site (B) are just 3% for rocking and 6.8% for sliding, almost identical in both fixed-based orientations, implying the reduction of nonlinearity observed during these analyses.

Figures 13a and 13b presents the resultant sliding and rocking for MC FN SSI cases at Sites (A) and (B). In this case, the responses observed at Site (A) demonstrate increased complexity due to the kinematic and inertial interactions of the SSI effect. Unlike the No-SSI case, three of the four casks on the two edges exhibit minimal rocking and sliding. One of the two casks in the center of the foundation pad displays moderate sliding with substantial rocking, while the other shows reduced sliding and rocking magnitudes. Site (B) exhibits arbitrary DSC

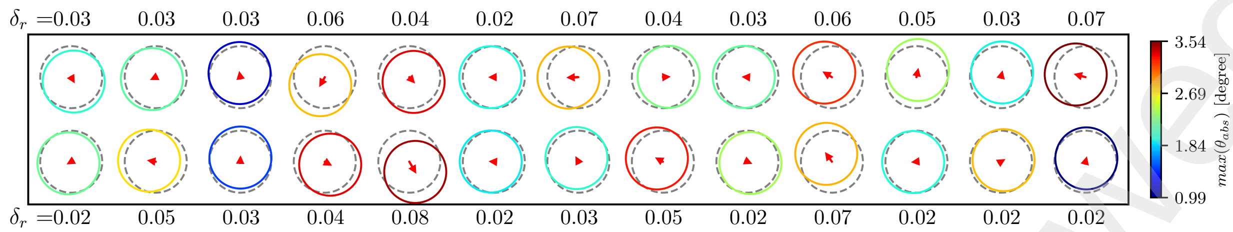

(a) Site (A)

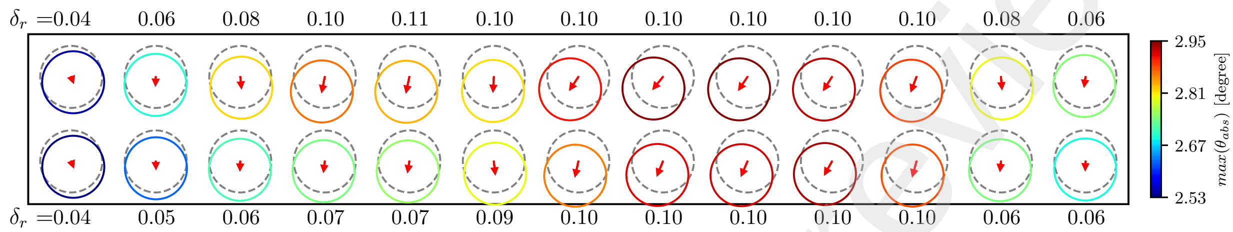

(b) Site (B)

Figure 13: Plan view: maximum resultant sliding vectors (δ_r, visualized with DSF 8) and maximum rocking responses ($max(\theta_{abs})$) of DSCs for FN SSI case.

responses, though no significant variability is detected in the rocking. Similar to the MC FN SSI in site (A), peripheral casks demonstrate reduced sliding and rocking responses.

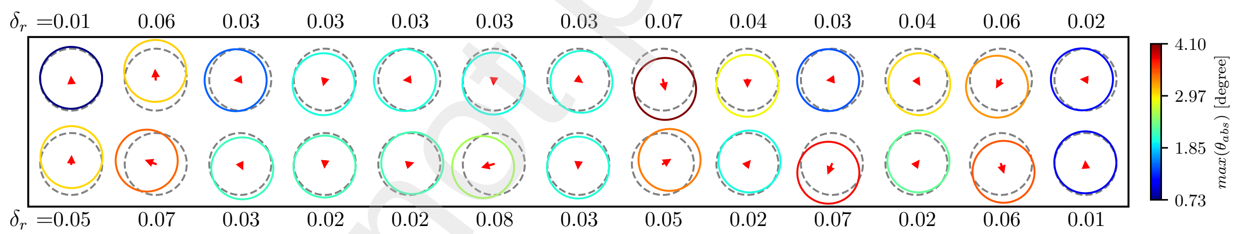

(a) Site (A)

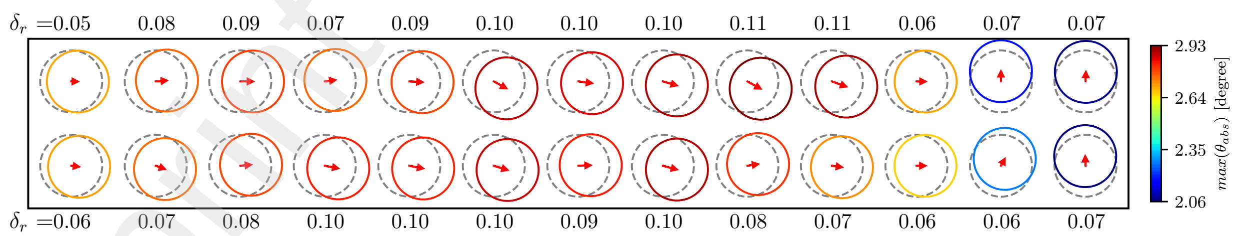

(b) Site (B)

Figure 14: Plan view: maximum resultant sliding vectors (δ_r, visualized with DSF 8) and maximum rocking responses ($max(\theta_{abs})$) of DSCs for FP SSI case (transformed counter-clockwise).

The MC FP SSI configuration results are portrayed in Figures 14a and 14b for site (A) and (B).

Site (A), for this case, exhibits maximum sliding and rocking among all four configurations, with rocking values ranging from 0.73° to 4.10° and sliding values from 1.2cm to 7.8cm. The corresponding CV values (0.355 for rocking, 0.479 for sliding) are the highest among all tested configurations, indicating that FP SSI creates the most chaotic dynamic environment for DSCs. Site (B) shows slightly increased sliding compared to other cases, but reduced rocking compared to MC FN SSI. In addition, both sites reveal response patterns similar to those of MC FN SSI, which is characterized by arbitrary behavior.

To better visualize the differences between all the eight near-field cases, two separate box-and-whisker diagrams were generated for the maximum resultant sliding (Figure 15b) and absolute rocking values (Figure 15a) obtained in the previous plots.

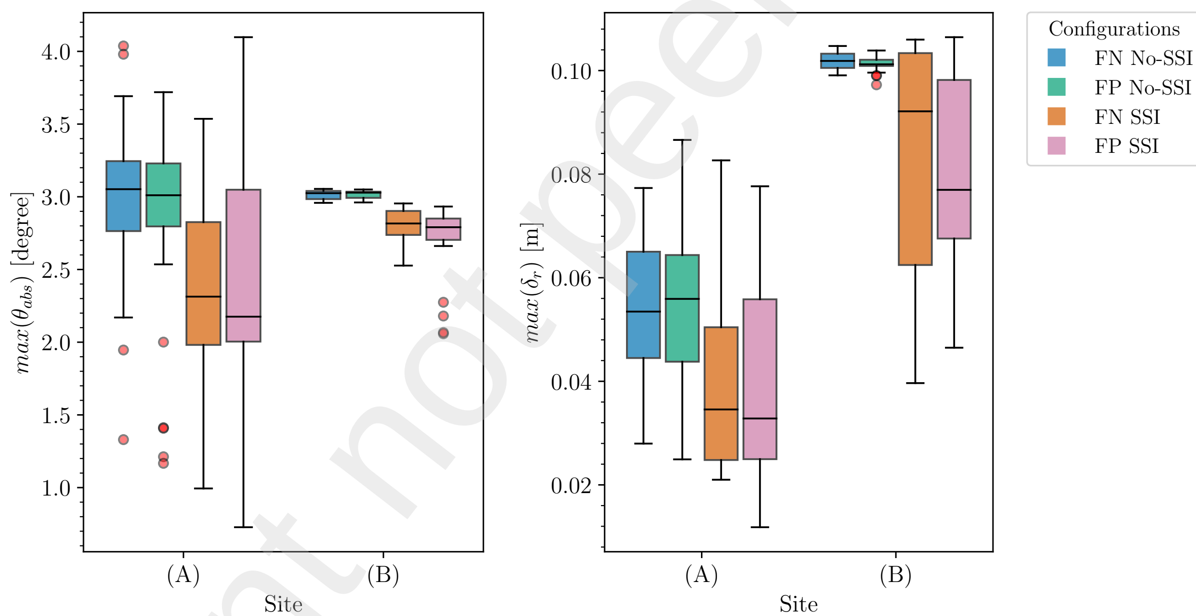

(a) (b)

Figure 15: Statistical distribution of (a) maximum absolute rocking and (b) maximum resultant sliding responses observed for the No-SSI and SSI cases for Sites A and B.

The analysis reveals noticeable differences in response characteristics between configurations, with Site (A) exhibiting greater rocking variability than Site (B) across all arrangements, while sliding behavior follows a more complex pattern. For rocking responses, the introduction of SSI reduces the median values while substantially increasing response variability – a pattern especially pronounced in the FP arrangements. Interestingly for sliding, Site (B) demonstrates higher variability than Site (A) when SSI is considered, with sliding interquartile range (IQR) values reaching 4.09cm (FN) and 3.06cm (FP) compared to Site (A)'s 2.56cm (FN) and 3.09cm (FP), suggesting that distance from fault influences rocking and sliding behaviors differently. Similarly for sliding at Site (A), though median responses decrease, significant variability emerges when transitioning from fixed-base to flexible-base conditions. The FP SSI configuration at Site (A) demonstrates the most extreme response diversity, with the rocking IQR almost doubling when transitioning from No-SSI FP to SSI FP (from 0.433° to 1.044°), while the sliding IQR increases from 2.1cm to 3.1cm. This indicates that even the middle 50% of casks experience substantially wider response variations under SSI conditions. These discussions suggest that incorporating SSI generally provides a damping effect on the overall magnitude of response while simultaneously introducing significant response variability and highlights the necessity of site-specific analyses for ISFSIs, specifically in the vicinity of faults.

Further, in spite of assigning an identical modeling assumptions and parameters for all casks, an arbitrary pattern in DSC responses can be noticed in Figures 11a, 12a, 13a and 14a for Site (A). This phenomenon aligns with the observations discussed by previous researchers [3, 9]. The chaotic behavior can be attributed to the nonlinear contact interactions between DSCs and the concrete pad during impact sequences [31], modal energy exchange between competing vibration modes [32], and extreme sensitivity to slight variation of response at a time instance [33]. The SSI cases (Figures 13a and 14a) exhibit even greater complexity due to a flexible base. In contrast, Site (B) demonstrates comparatively uniform, predictable response patterns despite having almost similar frequency content to Site (A) because of the reduced intensity of the input excitation, which remains below the critical velocity threshold required to drive the system into a chaotic regime [31, 32].

4 Conclusions

This study demonstrates the importance of fully 3D seismic wavefield simulations and advanced soil-structure interaction modeling for accurately predicting the seismic performance of dry storage casks. By coupling the DRM with PML boundaries and explicit finite element analyses in LS-DYNA, we were able to:

- Capture near-field complexities: Spatially varying ground motions in near-field sites resulted in pronounced rocking and sliding, with some casks exhibiting chaotic behavior and large displacements.
- Quantify far-field trends: Far-field simulations showed that DSC responses were closer to free-field motions, with negligible sliding and rocking due to reduced ground motion intensity.
- Highlight the influence of SSI: Inclusion of SSI effects led to altered responses relative to fixed-base scenarios, sometimes increasing variability in cask displacements and accelerations.
- Emphasizing the need for site-specific analysis: Multi-cask (MC) arrays, in particular, exhibited significant variability across individual casks, even when identical frictional properties and soil profiles were employed.

Overall, the findings underscore that simplified methods (e.g., one-dimensional deconvolution or rigid-base assumptions) may underestimate critical interactions that govern DSC performance in actual earthquakes. This research thus supports using more comprehensive, physics-based numerical frameworks for assessing seismic risks to DSCs.

5 Acknowledgments

This research is being performed using funding received from the DOE Office of Nuclear Energy's University Programs. All findings and conclusions discussed in this paper are those of the authors and do not reflect the Department of Energy's views.

6 Declaration

While preparing this work, the authors used Grammarly to improve language and readability. After using it, the authors reviewed and edited the content as needed, and they take full responsibility for the publication's content.

References

[1] Toshiari Saegusa, Koji Shirai, T. Arai, J. Tani, H. Takeda, M. Wataru, A. Sasahara, and P.L. Winston. Review and future issues on spent nuclear fuel storage. *Nuclear Engineering and Technology*, 42(3):237–248, June 2010. ISSN 1738–5733. doi:10.5516/net.2010.42.3.237.

[2] Moamen G. El-Samrah, A.F. Tawfic, and Samir E. Chidiac. Spent nuclear fuel interim dry storage; design requirements, most common methods, and evolution: A review. *Annals of Nuclear Energy*, 160:108408, September 2021. ISSN 0306–4549. doi:10.1016/j.anucene.2021.108408.

[3] YungYen Ko, Hsuanchih Yang, and Chin-Cheng Huang. An investigation of the seismic response of a free-standing dry storage cask for spent fuel using the finite element method. *Nuclear Engineering and Design*, 261:33–43, August 2013. ISSN 0029–5493. doi:10.1016/j.nucengdes.2013.03.021.

[4] Seungpil Kim and Sang Soon Cho. Seismic analysis of free-standing spent-fuel dry storage

cask considering soil–concrete pad-cask interaction. *Nuclear Engineering and Technology*, 56(10):4446–4454, October 2024. ISSN 1738–5733. doi:10.1016/j.net.2024.06.006.

[5] Vincent K. Luk, Benjamin Whiting Spencer, Ignatius Po Lam, and Robert A. Dameron. Parametric evaluation of seismic behavior of freestanding spent fuel dry cask storage systems. Technical Report NUREG/CR-6865, SAND2004-5794P, Division of Engineering Technology, Office of Nuclear Regulatory Research, U.S. Nuclear Regulatory Commission, Washington, DC 20555-0001, February 2005. NRC Job Code W6829. Available at: www.nrc.gov/reading-rm/doc-collections/nuregs/contract/cr6865/.

[6] Sharad Dangol and Luis Ibarra. Effect of vertical accelerations on dry storage cask seismic performance. In *Transactions of the 22nd International Conference on Structural Mechanics in Reactor Technology (SMiRT 22)*, volume III – Applied Computation Simulation and Animation, pages 1–10, San Francisco, CA, August 2013. International & American Associations for Structural Mechanics in Reactor Technology (IASMiRT), IASMiRT. URL www.lib.ncsu.edu/resolver/1840.20/32863.

[7] Gordon S. Bjorkman, Jr., Donald P. Moore, Jeffrey J. Nolin, and Victor J. Thompson. Influence of ISFSI design parameters on the seismic response of dry storage casks. In *Transactions of the 16th International Conference on Structural Mechanics in Reactor Technology (SMiRT 16)*, volume W - Decommissioning of Nuclear Facilities and Waste Management, pages 1–8, Washington, DC, August 2001. International & American Associations for Structural Mechanics in Reactor Technology, IASMiRT. URL www.lib.ncsu.edu/resolver/1840.20/30933.

[8] Goodluck I. Ofoegbu and G. Douglas Gute. Dynamic soil-structure interaction analysis of a storage-cask foundation design. Technical Report CNWRA 2003-03, Center for Nuclear Waste Regulatory Analyses, NRC Office of Nuclear Material Safety and Safeguards, Spent Fuel Project Office, U.S. Nuclear Regulatory Commission, San Antonio, Texas,

2002. Prepared for U.S. Nuclear Regulatory Commission, Contract NRC-02-97-009. Available at: www.nrc.gov/docs/ML0336/ML033640101.pdf.

[9] Sharad Dangol, Luis Ibarra, Steven Bartlett, Chris Pantelides, and David Sanders. Soil effects on the response of free-standing dry storage casks. In *Proceedings of 16th European Conference on Earthquake Engineering (16ECEE)*, pages 1–13, Thessaloniki, Greece, June 2018. Hellenic Society of Earthquake Engineering.

[10] Majid Ebad Sichani, Jamie E. Padgett, and Vahid Bisadi. Probabilistic seismic analysis of concrete dry cask structures. *Structural Safety*, 73:87–98, July 2018. ISSN 0167-4730. doi:10.1016/j.strusafe.2018.03.001.

[11] Majid Ebad Sichani, Mohammad Hanifehzadeh, Jamie E. Padgett, and Bora Gencturk. Probabilistic analysis of vertical concrete dry casks subjected to tip-over and aging effects. *Nuclear Engineering and Design*, 343:232–247, March 2019. ISSN 0029-5493. doi:10.1016/j.nucengdes.2018.12.003.

[12] Vincent K. Luk, Benjamin Whiting Spencer, Syed Khalid Shaukat, Ignatius Po Lam, and Robert A. Dameron. Sensitivity analyses of seismic behavior of spent fuel dry cask storage systems. In *Transactions of the 17th International Conference on Structural Mechanics in Reactor Technology (SMiRT 17)*, K - Seismic Analysis, Design and Qualification of Equipment, pages 1–8, Prague, Czech Republic, August 2003. International & American Associations for Structural Mechanics in Reactor Technology (IASMiRT). URL www.lib.ncsu.edu/resolver/1840.20/27322.

[13] Yung-Yen Ko, Shang-Yi Hsu, and Cheng-Hsing Chen. Analysis for seismic response of dry storage facility for spent fuel. *Nuclear Engineering and Design*, 239(1):158–168, January 2009. ISSN 0029–5493. doi:10.1016/j.nucengdes.2008.09.006.

[14] Nicholas Callahan, Charles Papadelis, Paul Wilson, George G. Thomas, and Mrinal Bose. Effects of isfsi pad flexibility on soil structure interaction (ssi) analysis. In *Proceedings*

of the 22nd International Conference on Structural Mechanics in Reactor Technology (SMiRT 22), IX - Fuel Cycle Facilities Waste Management and Decommissioning, pages 18–23, San Francisco, CA, August 2013. International & American Associations for Structural Mechanics in Reactor Technology (IASMiRT). URL www.lib.ncsu.edu/resolver/1840.20/33148.

[15] David McCallen, Anders Petersson, Arthur Rodgers, Arben Pitarka, Mamun Miah, Floriana Petrone, Björn Sjögreen, Norman Abrahamson, and Houjun Tang. EQSIM–a multidisciplinary framework for fault-to-structure earthquake simulations on exascale computers part I: Computational models and workflow. *Earthquake Spectra*, 37(2): 707–735, December 2020. ISSN 1944–8201. doi:10.1177/8755293020970982.

[16] N. Anders Petersson and Björn Sjögreen. User's guide to SW4, version 2.0. Technical Report LLNL-SM-741439, Center for Applied Scientific Computing, Lawrence Livermore National Laboratory, 7000 East Ave., Livermore, CA 94550, 2017. Available at: https://geodynamics.org/resources/1767/download/SW4-UsersGuide-2.0.pdf.

[17] David McCallen, Arben Pitarka, Houjun Tang, Ramesh Pankajakshan, Anders Petersson, and Mamun Miah. Transformational regional-scale earthquake simulations with the doe earthquake simulation exascale framework. *Computing in Science & Engineering*, 26(2): 16–24, April 2024. ISSN 1558–366X. doi:10.1109/mcse.2024.3397768.

[18] Floriana Petrone, Norman Abrahamson, David McCallen, and Mamun Miah. Validation of (not-historical) large-event near-fault ground-motion simulations for use in civil engineering applications. *Earthquake Engineering & Structural Dynamics*, 50(1):116–134, October 2020. ISSN 1096–9845. doi:10.1002/eqe.3366.

[19] David McCallen, Floriana Petrone, Mamun Miah, Arben Pitarka, Arthur Rodgers, and Norman Abrahamson. EQSIM–a multidisciplinary framework for fault-to-structure earthquake simulations on exascale computers, part II: Regional simulations of build-

ing response. *Earthquake Spectra*, 37(2):736–761, December 2020. ISSN 1944–8201. doi:10.1177/8755293020970980.

[20] Robert Graves and Arben Pitarka. Kinematic ground motion simulations on rough faults including effects of 3D stochastic velocity perturbations. *Bulletin of the Seismological Society of America*, 106(5):2136–2153, August 2016. doi:10.1785/0120160088.

[21] Arben Pitarka, Robert Graves, Kojiro Irikura, Ken Miyakoshi, Changjiang Wu, Hiroshi Kawase, Arthur Rodgers, and David McCallen. Refinements to the Graves-Pitarka kinematic rupture generator, including a dynamically consistent slip-rate function, applied to the 2019 Mw 7.1 ridgecrest earthquake. *Bulletin of the Seismological Society of America*, 112(1):287–306, October 2021. doi:10.1785/0120210138.

[22] LSTC. *LS-DYNA Keyword User's Manual, Volume I*. ANSYS Inc., Canonsburg, PA, USA, R14@841bce8cd edition, November 2023. URL `https://lsdyna.ansys.com/manual/`. Version: R14, November 28, 2023.

[23] Ushnish Basu and Anil K. Chopra. Perfectly matched layers for time-harmonic elastodynamics of unbounded domains: theory and finite-element implementation. *Computer Methods in Applied Mechanics and Engineering*, 192(11):1337–1375, 2003. ISSN 0045–7825. doi:10.1016/S0045-7825(02)00642-4.

[24] Ushnish Basu. Explicit finite element perfectly matched layer for transient three-dimensional elastic waves. *International Journal for Numerical Methods in Engineering*, 77(2):151–176, 2009. doi:10.1002/nme.2397.

[25] Elena Kalinina and Lucas Lujan. Friction experiment data analysis. Technical Report SAND-2023-11569R, Sandia National Laboratories, Albuquerque, NM, January 2023. URL `www.osti.gov/biblio/2432067`.

[26] G. Gazetas, E. Garini, I. Anastasopoulos, and T. Georgarakos. Effects of near-fault ground

shaking on sliding systems. *Journal of Geotechnical and Geoenvironmental Engineering*, 135(12):1906–1921, December 2009. doi:10.1061/(asce)gt.1943-5606.0000174.

[27] Elena Kalinina, Douglas Ammerman, Lucas Lujan, and Gregg Flores. Updated seismic shake table test plan. Technical Report SAND2022-10304R; 708802; TRN:US2308746, Sandia National Laboratories, Albuquerque, NM, July 2022. URL www.osti.gov/biblio/1879615. Milestone Number M2SF-22SN010202022.

[28] U.S. Nuclear Regulatory Commission. Regulatory guide 1.60: Design response spectra for seismic design of nuclear power plants, July 2014. URL https://www.nrc.gov/docs/ML1321/ML13210A432.pdf. Revision 2.

[29] Nathan M. Newmark and W. J. Hall. Development of criteria for seismic review of selected nuclear power plants. Technical Report NUREG CR–0098, U.S. Nuclear Regulatory Commission, Washington, D.C., May 1978. URL https://www.nrc.gov/docs/ML1921/ML19210C166.pdf.

[30] R. K. McGuire, W. J. Silva, and C. J. Costantino. Technical basis for revision of regulatory guidance on design ground motions: Hazard- and risk-consistent ground motion spectra guidelines. Technical Report NUREG CR–6728, U.S. Nuclear Regulatory Commission, Washington, D.C., November 2001. URL https://www.nrc.gov/docs/ML0131/ML013100232.html.

[31] ManYong Jeong, Kohei Suzuki, and Solomon C.S Yim. Chaotic rocking behavior of freestanding objects with sliding motion. *Journal of Sound and Vibration*, 262(5): 1091–1112, May 2003. ISSN 0022–460X. doi:10.1016/s0022-460x(02)01087-8.

[32] Francesco Pellicano and Marco Barbieri. Complex dynamics of circular cylindrical shells. *International Journal of Non-Linear Mechanics*, 65:196–212, October 2014. ISSN 0020–7462. doi:10.1016/j.ijnonlinmec.2014.05.006.

[33] Antonios A. Katsamakas and Michalis F. Vassiliou. Finite element modeling of free-standing cylindrical columns under seismic excitation. *Earthquake Engineering & Structural Dynamics*, 51(9):2016–2035, May 2022. ISSN 1096–9845. doi:10.1002/eqe.3651.